

Luminosity Functions of Local Infrared Galaxies with the AKARI: Implications to the Cosmic Star Formation History and AGN Evolution

Tomotsugu Goto^{1,2}, * Stephane Arnouts³, Hanae Inami⁴, Hideo Matsuhara⁵, Chris Pearson⁶, Tsutomu T. Takeuchi⁷, Emeric Le Floc'h⁸, Toshinobu Takagi, Takehiko Wada, Takao Nakagawa⁵, Shinki Oyabu², Daisuke Ishihara⁷, Hyung Mok Lee⁹, Woong-Seob Jeong¹⁰, Chisato Yamauchi⁵, S. Serjeant, C. Sedgwick¹¹, and Ezequiel Treister¹

¹*Institute for Astronomy, University of Hawaii, 2680 Woodlawn Drive, Honolulu, HI, 96822, USA*

²*Subaru Telescope 650 North A'ohoku Place Hilo, HI 96720, USA*

³*Canada France Hawaii Telescope, 65-1238 Mamalahoa Hwy, Kamuela, Hawaii 96743 USA*

⁴*Spitzer Science Center, California Institute of Technology, Pasadena, CA 91125, USA*

⁵*Institute of Space and Astronautical Science, Japan Aerospace Exploration Agency, Sagamihara, Kanagawa 252-5210*

⁶*Rutherford Appleton Laboratory, Chilton, Didcot, Oxfordshire OX11 0QX, UK*

⁷*Institute for Advanced Research, Nagoya University, Furo-cho, Chikusa-ku, Nagoya 464-8601*

⁸*CEA-Saclay, Service d'Astrophysique, France*

⁹*Department of Physics & Astronomy, FPRD, Seoul National University, Shillim-Dong, Kwanak-Gu, Seoul 151-742, Korea*

¹⁰*Korea Astronomy and Space Science Institute 61-1, Hwaam-dong, Yuseong-gu, Daejeon, Republic of Korea 305-348*

¹¹*Astrophysics Group, Department of Physics, The Open University, Milton Keynes, MK7 6AA, UK*

5 February 2022

ABSTRACT

Infrared (IR) luminosity is fundamental to understanding the cosmic star formation history and AGN evolution, since their most intense stages are often obscured by dust. However, local IR luminosity function estimates today are still based on the IRAS survey in the 1980s, with wavelength coverage only up to $100\mu\text{m}$. The AKARI IR space telescope performed all sky survey in 6 IR bands (9, 18, 65, 90, 140, and $160\mu\text{m}$) with 3-10 times better sensitivity, covering the crucial far-IR wavelengths across the peak of the dust emission. Combined with a better spatial resolution, AKARI can much more precisely measure the total infrared luminosity (L_{TIR}) of individual galaxies, and thus, the total infrared luminosity density in the local Universe.

By fitting modern IR SED models, we have re-measured L_{TIR} of the IRAS Revised Bright Galaxy Sample, which is a complete sample of local galaxies with $S_{60\mu\text{m}} > 5.24Jy$.

We present mid-IR monochromatic luminosity (νL_ν) to L_{TIR} correlations for Spitzer $8\mu\text{m}$, AKARI $9\mu\text{m}$, IRAS $12\mu\text{m}$, WISE $12\mu\text{m}$, ISO $15\mu\text{m}$, AKARI $18\mu\text{m}$, WISE $22\mu\text{m}$, and Spitzer $24\mu\text{m}$ filters. These measures of L_{MIR} are well correlated with L_{TIR} , with scatter ranging 13-44%. The best-fit L_{MIR} -to- L_{TIR} conversions provide us with estimates of L_{TIR} using only a single MIR band, in which several deep all sky surveys are becoming available such as AKARI MIR and WISE.

Although we found some overestimates of L_{TIR} by IRAS due to contaminating cirrus/sources, the resulting AKARI IR luminosity function (LF) agrees well with that from the IRAS. We integrate the LF weighted by L_{TIR} to obtain a cosmic IR luminosity density of $\Omega_{TIR} = (8.5_{-2.3}^{+1.5}) \times 10^7 L_\odot \text{Mpc}^{-3}$, of which $7 \pm 1\%$ is produced by LIRGs ($L_{TIR} > 10^{11} L_\odot$), and only $0.4 \pm 0.1\%$ is from ULIRGs ($L_{TIR} > 10^{12} L_\odot$) in the local Universe, in a stark contrast to high-redshift results.

We separate the contributions from AGN and star-forming galaxies (SFG). SFG IR LF shows a steep decline at the bright-end. Combined with high-redshift results from the AKARI NEP deep survey, these data show a strong evolution of $\Omega_{TIR}^{SFG} \propto (1+z)^{4.0 \pm 0.5}$, and $\Omega_{TIR}^{AGN} \propto (1+z)^{4.4 \pm 0.4}$. For Ω_{TIR}^{AGN} , the ULIRG contribution exceeds that from LIRG already by $z \sim 1$. A rapid evolution in both Ω_{TIR}^{AGN} and Ω_{TIR}^{SFG} suggests the correlation between star formation and black hole accretion rate continues up to higher redshifts. We compare the evolution of Ω_{TIR}^{AGN} to that of X-ray luminosity density. The $\Omega_{TIR}^{AGN} / \Omega_{X-ray}^{AGN}$ ratio shows a possible increase at $z > 1$, suggesting an increase of obscured AGN at $z > 1$.

1 INTRODUCTION

To understand the cosmic history of star formation and black hole growth, we must understand infrared (IR) emission; the more intense star formation, the more deeply it is embedded in the dust, hence, such star formation is not visible in UV but in the infrared. Similarly, AGN evolutionary scenarios predict that they are heavily obscured at their youngest, Compton-thick stage (Treister, Urry, & Virani 2009). The Spitzer and AKARI satellites revealed large amounts of infrared emission in the high-redshift Universe, showing strong evolution in the infrared luminosity density (Le Flocc’h et al. 2005; Pérez-González et al. 2005; Babbedge et al. 2006; Caputi et al. 2007; Magnelli et al. 2009). For example, at $z=1$, Goto et al. (2010) estimated 90% of star formation activity is hidden by dust. However, the key baseline of these evolution studies is still at $z=0$, using a local infrared LF from the IRAS survey in 1980s.

For more than 25 years, bolometric infrared luminosities ($L_{TIR,8-1000\mu m}$) of local galaxies have been estimated using a simple polynomial presented by Péruault (1987), obtained assuming a simple blackbody and dust emissivity. Furthermore, the reddest filter of IRAS is $100\mu m$, which does not span the peak of the dust emission for most galaxies, leaving a great deal of uncertainty. A number of studies found cold dust that cannot be detected with the IRAS. For example, Dunne & Eales (2001) detected such cold dust with $T \sim 20K$ using SCUBA $450,850\mu m$ observation. Symeonidis et al. (2009) detected cold galaxies with SED peaks at longer wavelengths using Spitzer/MIPS. These results cast further doubt on L_{TIR} estimation made with only $< 100\mu m$ photometry. More precise estimate of local L_{TIR} and thus the local IR luminosity function (LF) have been long awaited, to be better compared with high redshift work.

AKARI, the Japanese infrared satellite (Murakami et al. 2007), provides the first chance to rectify the situation since IRAS; AKARI performed an all-sky survey in two mid-infrared (centered on 9 and $18\mu m$) and four far-infrared bands ($65, 90, 140,$ and $160\mu m$). Its 140 and $160\mu m$ are especially important to cover across the peak of the dust emission, allowing us to accurately measure the Rayleigh-Jeans tail of the IR emission. The time is ripe in terms of modeling as well; several sophisticated infrared SED models have become available (Chary & Elbaz 2001; Dale & Helou 2002; Lagache, Dole, & Puget 2003; Siebenmorgen & Krügel 2007), from which we can not only obtain accurate L_{TIR} estimates, but also constrain the astrophysics.

In this work, we aim to re-measure local L_{TIR} , and thereby the IR LF of the Revised Bright Galaxy Sample (RBGS, Sanders et al. 2003), which is a complete sample of local IR galaxies. This work provides us an important local benchmark to base future evolution studies at high redshift both by the current AKARI and Spitzer satellites, and by next-generation IR satellites such as Herschel, WISE, JWST, and SPICA. We adopt a cosmology with $(h, \Omega_m, \Omega_\Lambda) = (0.75, 0.3, 0.7)$ for a comparison purpose.

2 THE AKARI ALL SKY SURVEY AND RBGS

In this work, we use the $\beta 1$ version of the AKARI/IRC bright source catalog and the $\beta 2$ version of the AKARI/FIS bright source catalog. The 5σ sensitivities in the AKARI IR filters ($S9W, L18W, N60, W5, WL$ and $N160$) are 0.05, 0.09, 2.4, 0.55, 1.4, and 6.3 Jy (Ishihara et al. 2010; Yamamura et al. 2009). In addition to the much improved sensitivity and spatial resolution

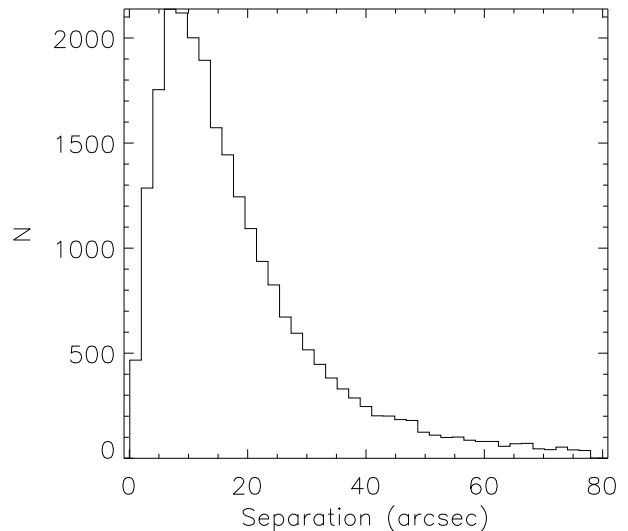


Figure 1. Angular separation between AKARI FIS and IRAS sources. We matched sources within 60 arcsec of separation.

over its precursor (IRAS), the presence of 140 and $160\mu m$ bands is crucial to measure the peak of the dust emission in the FIR wavelength, and thus the L_{TIR} of galaxies, especially ones with lower dust temperature.

We have cross-correlated the AKARI bright source catalog with the Revised Bright Galaxy Sample (RBGS; Sanders et al. 2003), using a matching radius of 60 arcsec, as shown in Fig.1. The RBGS is a complete, flux-limited survey of all extragalactic objects with $60\mu m$ flux density greater than $5.24Jy$, covering the entire sky at $|b| > 5$ deg. All 629 objects in this catalog have measured spectroscopic redshifts either from optical or millimeter/radio (CO or HI data). The maximum redshift of our sample is 0.087. Because of the completeness and availability of the spectroscopic redshifts, this catalog is suitable to construct local infrared luminosity functions (LFs). In addition, each galaxy has a measured IR luminosity from the IRAS survey, allowing us to compare with the AKARI-based one. Due to the difference in sky coverage (IRAS covers 96% of the sky, and AKARI covers 94%), 24 galaxies out of 629 RBGS galaxies did not have an AKARI counterpart. We removed these galaxies from our analysis, but applied corresponding completeness corrections to our statistical analysis.

One important caveat is that the RBGS is a flux-limited sample from IRAS ($S_{60\mu m} > 5.24Jy$). Therefore, if the IRAS $S_{60\mu m}$ flux was an overestimate as we discuss later, our work does not address incompleteness in the sample selection. However, at this very low-redshift (average redshift of 0.0082), the RBGS is still the largest complete sample of IR galaxies with spectroscopic redshift.

3 INFRARED LUMINOSITY

3.1 Estimating total IR luminosity

For these galaxies, we estimated new total IR luminosities (L_{TIR}) based on the AKARI photometry using the LePhare code¹ to

¹ <http://www.cfht.hawaii.edu/~arnouts/lephare.html>

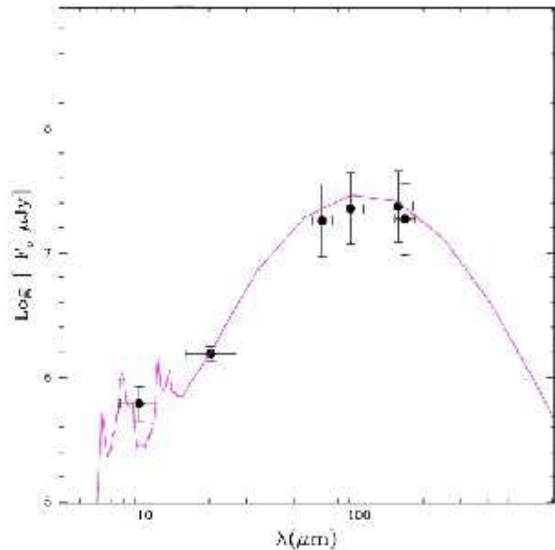


Figure 2. An example of the SED fit. We fit the AKARI 6-band photometry to the SED model of Chary & Elbaz (2001) to estimate L_{TIR} .

fit the infrared part ($>7\mu\text{m}$) of the SED and estimate TIR luminosity. We fit our AKARI FIR photometry with the SED templates from Chary & Elbaz (CHEL hereafter 2001). Although the shapes of these SEDs are luminosity-dependent, the large baseline from AKARI observations ($S9W, L18W, N60, WS, WL$ and $N160$) allows us to adopt a free scaling to get the best SED fit, which is then rescaled to derive L_{TIR} . Since the AKARI catalogs are the β -version, we adopted a minimum error of 25%. Fig.2 shows an example of the SED fit. At the median redshift of 0.0082 of the RBGS, peculiar velocity is not negligible. Therefore, instead of the measured redshift, we used the distance, which is corrected for heliocentric redshift using the cosmic attractor model (Mould et al. 2000) for the SED fitting and to compute L_{TIR} . In this work, L_{TIR} is measured in the wavelength range of 8-1000 μm .

We chose not to use IRAS 12,25,60 and 100 μm fluxes in the SED fitting. Due to the detector pixel size, AKARI has significantly better spatial resolution (30-40'') than IRAS (1-2'). In a few % of cases, AKARI measured significantly lower flux than the IRAS, because AKARI can subtract the background cirrus better, and/or can separate nearby confusing sources better. (See Jeong et al. (2007) for more details.)

In Fig.3, we compare L_{TIR} measured by AKARI with those by IRAS. The IRAS-based L_{TIR} is measured using the following equation.

$$L_{TIR}(L_{\odot}) \equiv 4.93 \times 10^{-22} [13.48L_{\nu}(12\mu\text{m}) + 5.16L_{\nu}(25\mu\text{m}) + 2.58L_{\nu}(60\mu\text{m}) + L_{\nu}(100\mu\text{m})] (\text{ergs}^{-1}\text{Hz}^{-1})$$

This equation is obtained by fitting a single temperature dust emissivity model ($\epsilon \propto \nu^{-1}$) to the flux in all four IRAS bands and should be accurate to $\pm 5\%$ for dust temperatures in the range of 25-65K (P  rault 1987). The L_{TIR} measured by AKARI agrees well with those by IRAS. However, the scatter increases toward lower luminosity in L_{TIR} measured by AKARI than by IRAS, especially at $\log(L_{TIR}) < 10$. This is primarily because AKARI's higher spatial resolution can separate background cirrus or confusing sources better than IRAS, resulting in lower L_{TIR} .

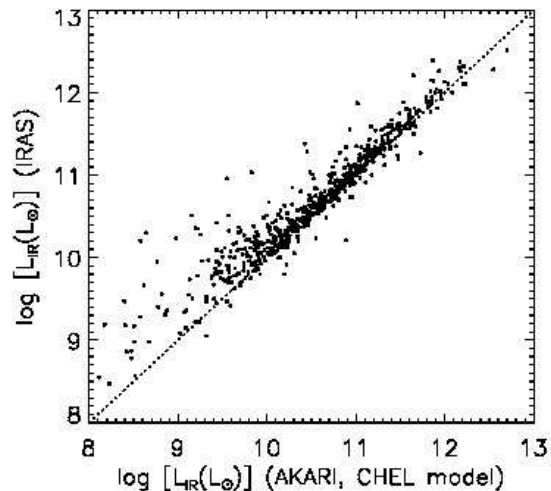


Figure 3. L_{TIR} measured by the AKARI is compared with those measured by the IRAS (Eq.1) for the RBGS.

Table 1. Comparison of L_{TIR} estimates with different SED models (Chary & Elbaz 2001; Dale & Helou 2002; Lagache, Dole, & Puget 2003). Fig.4 presents corresponding plots.

Models	σ (%)	Offset (%)
CHEL vs IRAS	44	-23
Dale vs Lagache	24	24
Dale vs CHEL	10	11
Lagache vs CHEL	22	-13

3.2 Model-to-model variation

In this section, we check the SED model dependence of L_{TIR} measurements. The IR SED models we used are Chary & Elbaz (2001); Dale & Helou (2002); Lagache, Dole, & Puget (2003). We used these models to compute L_{TIR} exactly as described in Section 3.1. In Fig.4, we plot the measured L_{TIR} against the model results, and find a tight correlation. As shown in Table 1, the standard deviations between different L_{TIR} s are 10-24%. The agreements are quite good considering the large flux errors ($\sim 25\%$) associated with infrared photometry. Median offsets between them are $-13 \sim +24\%$, which could also be caused by calibration problems. In Table 1, the CHEL model shows smallest offsets from other models. For k-correction and for L_{TIR} estimation (Section 3.1), we adopt CHEL models, which give luminosities in between the Dale models (11% higher) and Lagache models (13% lower).

Overall, there are good agreements between models, suggesting that once you have FIR photometry (WL and $N160$ in this work), the model-dependent uncertainty in L_{TIR} is small. This justifies our use of a single SED library for the final L_{TIR} measurement.

3.3 MIR- L_{TIR} correlation

A good correlation between Mid-IR monochromatic luminosity and L_{TIR} is known to exist. This is especially true for SF galaxies because the rest-frame MIR luminosity is dominated by prominent PAH features such as at 6.2, 7.7 and 8.6 μm , and the L_{TIR} is by

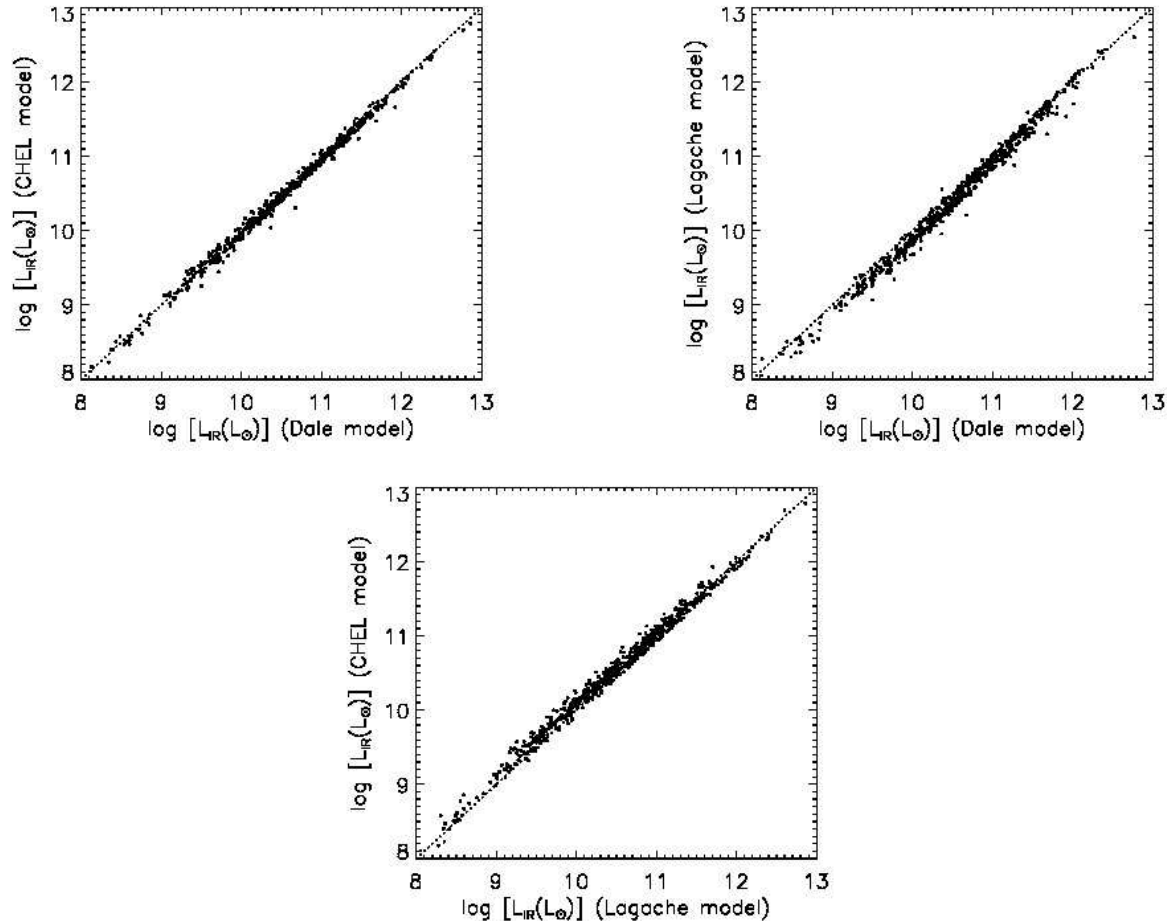


Figure 4. Comparing L_{TIR} measured using three different SED models (Chary & Elbaz 2001; Dale & Helou 2002; Lagache, Dole, & Puget 2003). Scatter and offsets between the models are summarized in Table 1.

dust emission heated by the SF activity; i.e., both of these are good indicators of SF activity. Observationally MIR detectors are more sensitive than in the FIR. Therefore, if we obtain accurate conversions from MIR to L_{TIR} , they will bring L_{TIR} measurement to much more galaxies.

AKARI covers both the MIR and FIR range with its 6 band-passes, measuring both MIR and total luminosity well. In addition, because it is an all-sky survey, it provides the 6-band photometry for ~ 600 RBGS galaxies. Here we have one of the best opportunities to investigate the L_{MIR} - L_{TIR} correlation.

We compute the MIR monochromatic luminosity at 8, 9, 12, 15, 18, 22, and 24 μm using the AKARI photometry at 9 and 18 μm , and the best-fit CHEL model from Section 3.1. For the definitions of monochromatic luminosity, we tried to choose luminosity in passbands of existing IR satellites, for precise and easily-reproducible definition, at the same time avoiding narrow emission/absorption features adding too much noise to the resulting relation. In addition, this choice allows users to apply the relations easily to observed fluxes, at least for low-redshift galaxies whose k-correction is small. We checked this choice of monochromatic filters did not have much effect compared to the exact luminosity at a certain single wavelength. We later show that MIR- L_{TIR} correlations for $WISE12\mu\text{m}$ and $IRAS12\mu\text{m}$ are almost identical. Our choices of filters are Spitzer 8 μm , AKARI 9 μm , IRAS

12 μm , WISE 12 μm , ISO 15 μm , AKARI 18 μm , WISE 22 μm , and Spitzer 24 μm .

For $L_{Spitzer8\mu\text{m}}$, $L_{AKARI9\mu\text{m}}$, $L_{IRAS12\mu\text{m}}$ and $L_{WISE12\mu\text{m}}$, we started from the observed 9 μm flux, then used the best-fit SED (to the 6 bands) from the CHEL model (§ 3.1) to color-correct the observed AKARI 9 μm flux to L_{MIR} in each filter. To be specific, we computed $L_{Spitzer8\mu\text{m}}$, $L_{AKARI9\mu\text{m}}$, $L_{IRAS12\mu\text{m}}$ and $L_{WISE12\mu\text{m}}$ through the filter response function of the Spitzer/IRAC 8 μm , the AKARI 9 μm , the IRAS 12 μm , and WISE 12 μm filters. Here, the best-fit model is only used to color-correct the observed 9 μm flux, and thus, the obtained L_{MIR} is not an integration of flux of the best-fit model.

Similarly, for $L_{ISO15\mu\text{m}}$, $L_{AKARI18\mu\text{m}}$, $L_{WISE22\mu\text{m}}$, and $L_{Spitzer24\mu\text{m}}$, we started from the observed AKARI 18 μm flux, color-corrected the flux using the color-correction from the best-fit SED model in § 3.1, then converted them to luminosity in each passbands. This color-correction is very small ($\sim 1\%$ at most) because AKARI's 9 and 18 μm are very close to other passbands. Thus, the results in Fig.5 show almost observed mid-IR luminosity against observed L_{TIR} .

In Fig.5, we show monochromatic luminosity in 8,9,12,15,18, 22 and 24 μm against L_{TIR} measured using the CHEL model. In Fig.5, there exist good correlations in each panel. In fact, the correlations look like a simple scaling relation in all panels, i.e., the

stronger the MIR-emission, the larger the L_{TIR} . The results suggest indeed monochromatic luminosity in mid-IR range represents the L_{TIR} well.

We fit a linear equation to the relation obtaining the following results. Note that the unit is in solar luminosity.

The best-fit relation between $L_{8\mu m}$ and L_{TIR} is

$$L_{TIR} = (20 \pm 5) \times \nu L_{\nu, 8\mu m}^{0.94 \pm 0.01} (\pm 44\%). \quad (2)$$

The best-fit relation between $L_{12\mu m}$ and L_{TIR} is

$$L_{TIR} = (17 \pm 4) \times \nu L_{\nu, 12\mu m}^{0.96 \pm 0.01} (\pm 25\%). \quad (3)$$

The best-fit relation between $L_{15\mu m}$ and L_{TIR} is

$$L_{TIR} = (24 \pm 8) \times \nu L_{\nu, 15\mu m}^{0.96 \pm 0.01} (\pm 13\%). \quad (4)$$

The best-fit relation between $L_{24\mu m}$ and L_{TIR} is

$$L_{TIR} = (51 \pm 19) \times \nu L_{\nu, 24\mu m}^{0.91 \pm 0.01} (\pm 24\%). \quad (5)$$

The logarithmic slopes of the relations are very similar to each other, perhaps reflecting the fact that most of these IR filters are wide and have some overlaps in wavelength coverage. This also means in this wavelength range (8-24 μm), and within broad filters, the SED shape does not depend much on L_{TIR} . However this result is at low redshift, and whether this applies at higher redshift needs to be examined separately. We note that $L_{\nu, 15\mu m}$ shows a less dispersed relation with L_{TIR} .

For $L_{8\mu m}$, Caputi et al. (2007) (eq.6), Bavouzet et al. (2008) (eq.7), and Boquien et al. (2010) (eq.8) present a correlation.

$$L_{TIR} = 1.91 \times (\nu L_{\nu})_{rest 8\mu m}^{1.06} (\pm 55\%) \quad (6)$$

$$L_{TIR} = 377.9 \times (\nu L_{\nu})_{rest 8\mu m}^{0.83} (\pm 37\%) \quad (7)$$

$$L_{TIR} = 216.9 \times (\nu L_{\nu})_{PAH 8\mu m}^{0.836} (\pm 29\%) \quad (8)$$

Note that for Boquien et al. (2010), we used their conversion in Table 1 from SINGS data. The unit is also converted from W to L_{\odot} . We overplot these relations in Fig.5. There is good agreement between these conversions and our best-fit relation, especially at $9 < \log L_{TIR} < 11$, where both samples have enough number of galaxies. Note that Caputi et al. (2007)'s sample spans at $0 < z < 0.6$ and Bavouzet et al. (2008)'s is mostly at $z \leq 0.4$. Thus, these samples are significantly at higher redshifts than ours. SED evolution could cause a small difference. See Boquien et al. (2010) for metallicity dependence of the conversion.

For $L_{12\mu m}$, there exists a conversion from Takeuchi et al. (2005).

$$\log L_{TIR} = 1.02 + 0.972 \log L_{12\mu m}, \quad (9)$$

We overplot the relation in Fig.5. The slope is in good agreement. There is a $\sim 50\%$ offset in zero points. Possible reasons of this offsets include different definition in $L_{12\mu m}$ and different estimates for L_{TIR} . Our $L_{12\mu m}$ relation is virtually identical to the one given by Spinoglio et al. (1995) which is, in our units:

$$\log L_{TIR} = 1.51 + 0.942 \log L_{12\mu m}, \quad (10)$$

For $L_{24\mu m}$, we compare the conversions with the following in the literature (Boquien et al. 2010; Bavouzet et al. 2008).

$$L_{TIR} = 57.9 \times (\nu L_{\nu})_{24\mu m}^{0.923} (\pm 54\%) \quad (11)$$

$$L_{TIR} = 6856 \times (\nu L_{\nu})_{24\mu m}^{0.71} (\pm 54\%) \quad (12)$$

Our conversion is in very good agreement with Boquien et al.

(2010). Bavouzet et al. (2008)'s relation has a slightly shallower slope, but in good agreement at $9 < \log L_{TIR} < 11$, where most of their galaxies lie.

Smith et al. (2007) observed 17 μm PAH complex features in Spitzer IRS spectra of nearby star-forming galaxies. This feature was not detected previously with ISO, and therefore not included in the SED model we used. Although Smith et al. (2007)'s SED templates only contained two data points in the far-IR, and thus were not suitable for our purpose, we try to estimate how the 17 μm PAH complex features affect the $L_{15\mu m}$ - L_{TIR} conversion as follows. First, we remove a continuum from both of the spectra, (Chary & Elbaz 2001; Smith et al. 2007). Then we replace the 6-20 μm region of the Chary & Elbaz (2001)'s spectra by Smith et al. (2007). Here we scaled the spectrum so that the amplitude of the 12 μm PAH complex matches. Thus, this new templates keep the overall SED shape of Chary & Elbaz (2001), but have the 17 μm PAH complex features from Smith et al. (2007). We rerun the SED fit to estimate the $L_{15\mu m}$ - L_{TIR} conversion to find that L_{TIR} estimate (as a function of $L_{15\mu m}$) will be $\sim 3\%$ smaller if the 17 μm PAH complex features are included in the SED. Although the effect is smaller than the errors of the conversion, this indicates that future SED models need to include the 17 μm PAH complex features.

With current technology, detectors are much more sensitive in the mid-IR range than in the far-IR range. Therefore, once these correlations are assumed, they will provide a useful conversion to compute luminosities of many more galaxies, either at higher redshift or at a fainter flux level, from a single MIR flux. For example, the above relations can provide a total IR flux measurement for all sources from the AKARI MIR all sky survey, which has 3 times more sources than the FIR all sky survey. WISE will perform even deeper all sky survey in 3.4, 4.6, 12 and 22 μm in the near future (Wright 2008). For future use, we also provide $L_{12\mu m}$ - L_{TIR} , and $L_{22\mu m}$ - L_{TIR} conversions in WISE filters as follows, and also in Fig.5.

The best-fit relation between $L_{WISE12\mu m}$ and L_{TIR} is

$$L_{TIR} = (18 \pm 5) \times \nu L_{\nu, WISE12\mu m}^{0.96 \pm 0.01} (\pm 23\%). \quad (13)$$

The best-fit relation between $L_{WISE22\mu m}$ and L_{TIR} is

$$L_{TIR} = (53 \pm 20) \times \nu L_{\nu, 22\mu m}^{0.91 \pm 0.01} (\pm 25\%). \quad (14)$$

4 INFRARED LUMINOSITY FUNCTIONS

4.1 The $1/V_{max}$ method

With accurately measured L_{TIR} , we are ready to construct IR LFs. Since the RBGS is a flux-limited survey, we need to correct for a volume effect to compute LFs. We used the $1/V_{max}$ method (Schmidt 1968) for this. An advantage of the $1/V_{max}$ method is that it allows us to compute a LF directly from data, with no parameter dependence or a model assumption. A drawback is that it assumes a homogeneous galaxy distribution and thus is vulnerable to local over-/under-densities (Takeuchi, Yoshikawa, & Ishii 2000).

A comoving volume associated to any source of a given luminosity is defined as $V_{max} = V_{z_{max}} - V_{z_{min}}$, where z_{min} is the lower limit of the redshift and z_{max} is the maximum redshift at which the object could be seen given the flux limit of the survey. In this work, we set $z_{min}=0.0004$ since at a very small redshift, an error in redshift measurement is dominated by a peculiar motion, and thus, L_{TIR} also has a large error. This only removes 5 galaxies from the sample.

For the RBGS, the detection limit is IRAS $S_{60\mu m} = 5.24Jy$.

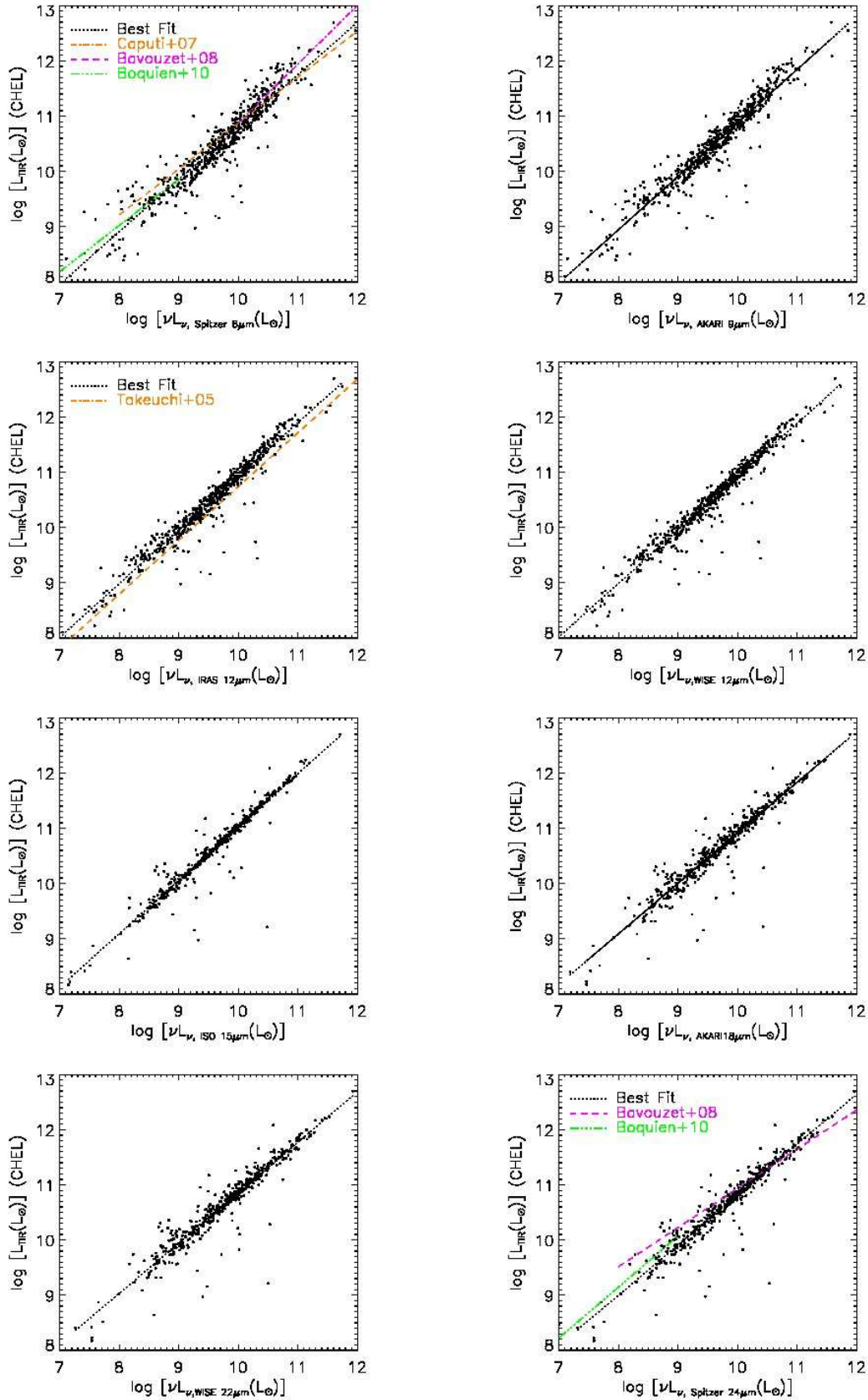


Figure 5. Correlations between L_{TIR} and monochromatic luminosities (8,9,12,15,18, 22 and 24 μm). The lines show the best-fit polynomial, based on which we present conversions. When available, conversions from the literature (Takeuchi et al. 2005; Caputi et al. 2007; Bavouzet et al. 2008; Boquien et al. 2010) are overplotted for a comparison.

We used the SED templates (Chary & Elbaz 2001) for k-correction to obtain the maximum observable redshift from the flux limit.

For each luminosity bin then, the LF is derived as

$$\phi = \frac{1}{\Delta L} \sum_i \frac{1}{V_{\max,i}} \quad (15)$$

,where V_{\max} is a comoving volume over which the i th galaxy could be observed, and ΔL is the size of the luminosity bin (0.3 dex). The RBGS is a complete in $60\mu\text{m}$ at IRAS $S_{60\mu\text{m}} > 5.24\text{Jy}$. Completeness correction in terms of sky coverage of both satellites is taken into account.

4.2 Monte Carlo simulation

Uncertainties in the LF values stem from various factors such as the finite numbers of sources in each luminosity bin, the k-correction uncertainties, and the flux errors. To compute these errors we performed Monte Carlo simulations by creating 1000 simulated catalogs, where each catalog contains the same number of sources, but we assign each source new fluxes following a Gaussian distribution centered at fluxes with a width of a measured error. Then we measured errors of each bin of the LF based from the variation in the 1000 simulations. These estimated errors are added in quadrature to the Poisson errors in each LF bin.

4.3 IR luminosity function

In Fig.6, we show LF of the RBGS but using AKARI photometry. Fig.7 shows number of galaxies used to compute the LF. The original LF measured using the IRAS photometry is also overplotted. There is a very good agreement between the LFs measured by AKARI and IRAS over the luminosity range of $8 < \log L_{TIR} < 12$. Although the IRAS-based L_{TIR} is computed using a single polynomial equation (Eq.1), the agreement shows it measured the IR LF very well. Perhaps, since a LF is an integrated quantity, it can be measured more reliably than L_{TIR} of individual galaxies, even using data up to only $100\mu\text{m}$.

Our LF in Fig.6 agrees well with Rush, Malkan and Spinoglio (1993), after correcting their results from a Hubble constant of 50 to 75. Their LF slightly underestimate LF, perhaps because they only integrated IRAS photometry up to $100\mu\text{m}$. Our LF also agrees well with Takeuchi, Yoshikawa, & Ishii (2003), once their $60\mu\text{m}$ LF is converted to L_{TIR} by multiplying 2.5 (Takeuchi et al. 2006). Their LF was measured in a SED model-free way, using different density estimators. It is reassuring that LFs measured in completely different ways agree well. See Sedgwick et al. (in prep.) for a similar attempt in the AKARI Deep field south.

Following Sanders et al. (2003), we fit an analytical function to the LFs. In the literature, IR LFs were fit better by a double-power law (Babbedge et al. 2006; Goto et al. 2010) or a double-exponential (Saunders et al. 1990; Pozzi et al. 2004; Takeuchi et al. 2006; Le Floc'h et al. 2005) than a Schechter function, which steeply declines at the high luminosity and underestimates the number of bright galaxies. In this work, we fit the TIR LFs using a double-power law (Babbedge et al. 2006).

$$\Phi(L)dL/L^* = \Phi^* \left(\frac{L}{L^*} \right)^{1-\alpha} dL/L^*, \quad (L < L^*) \quad (16)$$

$$\Phi(L)dL/L^* = \Phi^* \left(\frac{L}{L^*} \right)^{1-\beta} dL/L^*, \quad (L > L^*) \quad (17)$$

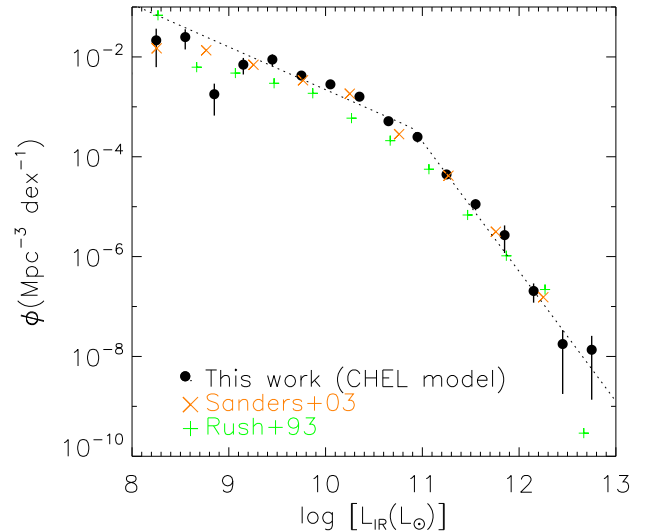


Figure 6. Infrared luminosity function of the RBGS. The L_{TIR} is measured using the AKARI 9,18,65,90,140 and $160\mu\text{m}$ fluxes through an SED fit. Errors are computed using 1000 Monte Carlo simulations, added by Poisson error. The dotted lines show the best-fit double-power law. The crosses show data from Sanders et al. (2003), who measured L_{TIR} using IRAS photometry. The plus show data from Rush, Malkan and Spinoglio (1993), who measured L_{FIR} by integrating IRAS fluxes over $12\text{--}100\mu\text{m}$.

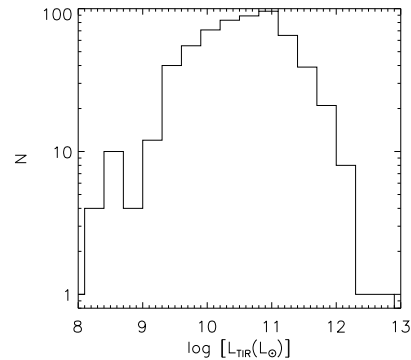


Figure 7. A luminosity histogram of galaxies used to compute Fig.6.

Free parameters are L^* (characteristic luminosity, L_\odot), ϕ^* (normalization, Mpc^{-3}), α , and β (faint and bright end slopes), respectively. The best-fit values are summarized in Table 2. The local LF has a break at $L^* = 7.8 \pm 0.2 \times 10^{10}$. Understanding how this break (L^*) evolves as function of cosmic time, and what causes the break is fundamental to galaxy evolution studies. This work provides an important benchmark in the local Universe.

4.4 Bolometric IR luminosity density based on the TIR LF

One of the primary purposes in computing IR LFs is to estimate the IR luminosity density, which in turn is a good estimator of the dust-hidden cosmic star formation density (Kennicutt 1998), provided the AGN contribution is removed. The bolometric IR luminosity of a galaxy is produced by thermal emission of its interstellar matter. In SF galaxies, the UV radiation produced by young stars heats

Table 2. Best double power-law fit parameters for the AKARI LFs, and the infrared luminosity density obtained from the fit

Sample	$L_{TIR}^* (L_{\odot})$	$\phi^* (\text{Mpc}^{-3} \text{dex}^{-1})$	α (faint-end)	β (bright-end)	$\Omega_{IR} (L_{\odot} \text{Mpc}^{-3})$
Total	$7.8 \pm 0.2 \times 10^{10}$	0.00037 ± 0.00005	1.8 ± 0.1	3.6 ± 0.1	$8.5^{+1.5}_{-2.3} \times 10^7$
SFG	$10 \pm 0.2 \times 10^{10}$	0.00018 ± 0.00006	1.9 ± 0.1	4.4 ± 0.3	$8.0^{+1.7}_{-2.5} \times 10^7$
AGN	$7.8 \pm 0.2 \times 10^{10}$	0.00011 ± 0.00005	1.7 ± 0.1	3.2 ± 0.3	$1.6^{+0.5}_{-0.3} \times 10^7$

the interstellar dust, and the reprocessed light is emitted in the IR. For this reason, in star-forming galaxies (SFG), the bolometric IR luminosity is a good estimator of the current SFR (star formation rate) of the galaxy.

Once we measured the LF, we can estimate the total infrared luminosity density by integrating the LF, weighted by the luminosity. We used the best-fit double-power law to integrate outside the luminosity range in which we have data, to obtain estimates of the total infrared luminosity density, Ω_{TIR} .

The resulting total luminosity density is $\Omega_{TIR} = (8.5^{+1.5}_{-2.3}) \times 10^7 L_{\odot} \text{Mpc}^{-3}$. Errors are estimated by varying the fit within 1σ of uncertainty in LFs. Out of Ω_{TIR} , $7 \pm 1\%$ is produced by LIRG ($L_{TIR} > 10^{11} L_{\odot}$), and only $0.4 \pm 0.1\%$ is by ULIRG ($L_{TIR} > 10^{12} L_{\odot}$). A very small fraction of Ω_{TIR} is produced by luminous infrared galaxies at $z=0.0082$, in stark contrast to high-redshift Universe. We found that $\sim 30\%$ of Ω_{TIR} originates from $L_{TIR} < 10^{8.2} L_{\odot}$, where we do not have data and had to rely on the extrapolation of the faint-end tail of the LF. Therefore, similar amount of uncertainty cannot be ruled out if the faint-end slope changes significantly under $L_{TIR} < 10^{8.2} L_{\odot}$. We will discuss the evolution of Ω_{TIR} in Section 5.2.

5 INFRARED LUMINOSITY DENSITY AND ITS EVOLUTION

5.1 Separating IR contributions from AGN and SFG

We showed a local IR LF in Fig.6. However this includes both IR emission from star formation activity and from AGN. Since different physics govern star formation and AGN, it is essential to separate their IR emission to understand the cosmic evolution of each component. For example, the cosmic star formation history cannot be addressed without subtracting the contribution from the AGN, and vice versa.

Separating AGN from starbursts is not a trivial task. Many AGN/SF separation methods have been proposed such as X-ray, radio luminosity, optical line ratios, PAH strengths, submm properties and so on, many of which often disagree with each other. We do not have a complete diagnosis of AGN/SB such as emission line ratios and X-ray for all of our sample. Therefore instead of classifying individual galaxies into AGN and SF, we attempt a statistical approach to separate contributions to LFs by AGN and star-forming galaxies.

In this work, we simply use a result of a new classification of Yuan, Kewley, & Sanders (2010), which used three carefully examined optical line ratio diagrams (Kewley et al. 2006) to classify individual galaxies. Based on optical line ratios they classify IR galaxies into AGN (LINER, Seyfert 1 and 2), star-forming, and composite as a function of L_{TIR} in their Table 4 and Figure 4. Their results agree well with other work (Takeuchi, Yoshikawa, & Ishii 2003; Goto 2005), within 20% or so. We use their fractions of AGN/SFG as a function of L_{TIR} ,

to separate our LF into that of AGN and SFG. In this process, it is an open question how to handle composite galaxies, which are close to 50% of galaxies in almost all bins. In this work, we simply assigned the AGN/SF fractional ratio of that luminosity bin to separate composite galaxies (and ambiguous galaxies) into AGN/SF galaxies. We understand this is not an ideal approach. There will be up to $\sim 50\%$ uncertainty if these composite galaxies are all AGN or SFG. It merely provides one method to separate IR LFs into those of AGN and SFG. A method to assess IR contribution by AGN and SFG is becoming realistic. For example, Gandhi et al. (2009) showed a tight correlation between nuclear $L_{12.3\mu\text{m}}$ and $L_{X\text{-ray}}$. In the near future, more realistic classification of composite galaxies will become possible. We show the resulting AGN fraction from this process as a function of L_{TIR} in Fig.8. At $L_{TIR} > 10^{12} L_{\odot}$, this procedure assigns 90% of IR luminosity to AGN. At $L_{TIR} < 10^{10} L_{\odot}$, the AGN fraction is 20% or less. This also agrees well with a recent measurement by Kartaltepe et al. (2010).

By applying this AGN/SF separation, in Fig.9 we show LFs separately for AGN and SFG. The total IR LF shown in Fig.6 is also shown for comparison. As expected from Fig.8, Fig.9 shows that at $L_{TIR} > 10^{12} L_{\odot}$, the AGN are responsible for almost all of the L_{TIR} , forming a very steep bright-end drop for the SFG LF. On the other hand, at $L_{TIR} < 10^{11} L_{\odot}$, SF galaxies explain most of the L_{TIR} .

Next, we fit a double-power law (Eqs. 16 and 17) to the AGN and SF IR LFs, exactly as we did for the total IR LF in Fig.6. The best-fit parameters are summarized in Table 2. The most notable difference is at the bright-end slope (β), where the AGN LF has a very shallow slope of $\beta=3.2 \pm 0.3$, while the SFG has a steep slope of $\beta=4.4 \pm 0.3$. As expected, the faint-end tail (α) is not much different, in fact, being consistent with each other within 1σ . The L^* of SFG becomes brighter due to the steepening of the bright-end slope.

The total infrared luminosities of AGN and SFG's were also measured in separated LF's by Rush, Malkan and Spinoglio (1993). Adding their Seyfert 1 and Seyfert 2 LF's, and correcting for different Hubble constant, they get somewhat lower AGN/SFG LF ratios than our overall value of $1.6 : 8.0$. Their methodology was simpler, and did not account for the population of LINER AGN in their $12\mu\text{m}$ -selected galaxy sample.

What do these differences in LFs bring to the IR luminosity density, Ω_{IR} , by AGN and SFG? We estimate the total infrared luminosity density by integrating the LFs weighted by the luminosity, separately for AGN and SFG. We used the double power law outside the luminosity range in which we have data, to obtain estimates of the total infrared luminosity density, Ω_{TIR} , for AGN and SFG.

The resulting total luminosity density (Ω_{IR}) is, $\Omega_{IR}^{SFG} = 8.0^{+1.7}_{-2.5} \times 10^7 L_{\odot} \text{Mpc}^{-3}$, and $\Omega_{IR}^{AGN} = 1.6^{+0.5}_{-0.3} \times 10^7 L_{\odot} \text{Mpc}^{-3}$, as summarized in Table 3. Errors are estimated by varying the fit within 1σ of uncertainty in LFs. These are also summarized in Table 2. The results show that among the total IR

Table 3. Local IR luminosity densities

Sample	$\Omega_{IR}^{SFG} (L_{\odot}\text{Mpc}^{-3})$	$\Omega_{IR}^{AGN} (L_{\odot}\text{Mpc}^{-3})$
Total	$(8.0^{+1.7}_{-2.5}) \times 10^7$	$(1.6^{+0.5}_{-0.3}) \times 10^7$
LIRG	$(3.8^{+0.4}_{-0.9}) \times 10^6$	$(2.1^{+0.6}_{-0.5}) \times 10^6$
ULIRG	$(1.5^{+1.0}_{-1.0}) \times 10^4$	$(12^{+5}_{-7}) \times 10^4$

luminosity density integrated over all the IR luminosity range, 83% ($\frac{\Omega_{IR}^{SFG}}{\Omega_{IR}^{AGN} + \Omega_{IR}^{SFG}}$) of IR luminosity density is emitted by the SFG, and only 16% ($\frac{\Omega_{IR}^{AGN}}{\Omega_{IR}^{AGN} + \Omega_{IR}^{SFG}}$) is by AGN at $z=0.0082$. The results shows that at low redshift ($z=0.0082$), majority of the IR luminosity density is emitted by the SFG. Therefore, even if you convert all the Ω_{IR} into SFR density, you will only overestimate by 20%. However, the situation is different at higher redshift, where a number of papers reported luminosity evolution in the IR LF (Pérez-González et al. 2005; Le Flocc'h et al. 2005; Magnelli et al. 2009). The AGN/SFG separation will have much larger effect and thus more important at higher redshift.

Once we have Ω_{IR}^{SFG} , we can estimate star formation density emitted in infrared light. The SFR and L_{TIR} is related by the following equation for a Salpeter IMF, $\phi(m) \propto m^{-2.35}$ between $0.1 - 100 M_{\odot}$ (Kennicutt 1998).

$$SFR[M_{\odot}\text{yr}^{-1}] = 1.72 \times 10^{-10} L_{TIR}[L_{\odot}] \quad (18)$$

By using this equation, we obtain SFR density = $1.3 \pm 0.2 \times 10^{-2} M_{\odot}\text{yr}^{-1}$.

If we limit our integration to ULIRG luminosity range ($L_{TIR} > 10^{12} L_{\odot}$), we obtain, $\Omega_{IR}^{SFG}(\text{ULIRG}) = (1.5^{+1.0}_{-1.0}) \times 10^4 L_{\odot}\text{Mpc}^{-3}$, and $\Omega_{IR}^{AGN}(\text{ULIRG}) = (12^{+5}_{-7}) \times 10^4 L_{\odot}\text{Mpc}^{-3}$. In other words, at ULIRG luminosity range, AGN explain 88% ($\frac{\Omega_{IR}^{AGN}(\text{ULIRG})}{\Omega_{IR}^{AGN}(\text{ULIRG}) + \Omega_{IR}^{SFG}(\text{ULIRG})}$) of IR luminosity, again showing the AGN dominance at the bright-end.

In the LIRG luminosity ($L_{TIR} > 10^{11} L_{\odot}$), results are $\Omega_{IR}^{SFG}(\text{LIRG}) = (3.8^{+0.4}_{-0.9}) \times 10^6 L_{\odot}\text{Mpc}^{-3}$, and $\Omega_{IR}^{AGN}(\text{LIRG}) = (2.1^{+0.6}_{-0.5}) \times 10^6 L_{\odot}\text{Mpc}^{-3}$. This shows AGN contribution is already down to 35% ($\frac{\Omega_{IR}^{AGN}(\text{LIRG})}{\Omega_{IR}^{AGN}(\text{LIRG}) + \Omega_{IR}^{SFG}(\text{LIRG})}$) of IR luminosity in the LIRG range.

5.2 Evolution of Ω_{IR}^{SFG}

We have separated the Ω_{IR}^{SFG} from Ω_{IR}^{AGN} . Now we are ready to examine the evolution of Ω_{SFR} without contribution from AGN. In Fig.10, we plot the evolution of Ω_{IR}^{SFG} as a function of redshift. Higher redshift results are taken from Goto et al. (2010), who also tried to exclude AGN using SED fitting to individual galaxies. Results from the Spitzer survey and GALEX survey are also plotted. The Ω_{IR}^{SFG} shows a strong evolution as a function of redshift. The best-fit linear relation is $\Omega_{IR}^{SFG} \propto (1+z)^{4.0 \pm 0.5}$. This is consistent with most of earlier work. For example, Le Flocc'h et al. (2005) obtained $\gamma = 3.9 \pm 0.4$ up to $z \sim 1$. Pérez-González et al. (2005) found $\gamma = 4.0 \pm 0.2$ from $z=0$ to 0.8. Babbedge et al. (2006) obtained $\gamma = 4.5^{+0.7}_{-0.6}$. Magnelli et al. (2009) obtained $\gamma = 3.6 \pm 0.4$ up to $z=1.3$. Rodighiero et al. (2010) found $\gamma = 3.8 \pm 0.4$ in the redshift interval of $0 < z < 1$. Gruppioni et al. (2010) found $\gamma = 3.8 \pm 0.3$ up to $z \sim 1$, with some evidence of flattening up to $z \sim 2$.

Once the IR luminosity density is separated into ULIRG and LIRG contribution, we found $\Omega_{IR}^{SFG}(\text{ULIRG}) \propto (1+z)^{9.1 \pm 0.8}$,

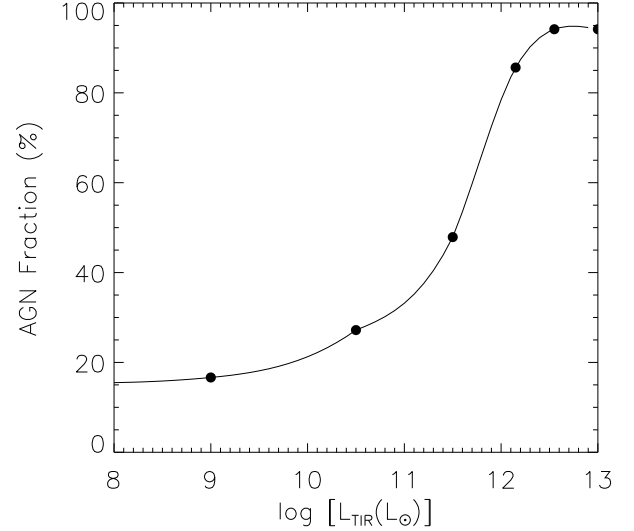


Figure 8. Fractions of AGN is shown as a function of L_{TIR} . The original classification was taken from Fig.4 of Yuan, Kewley, & Sanders (2010), and interpolated by a spline curve to be applied to our LFs.

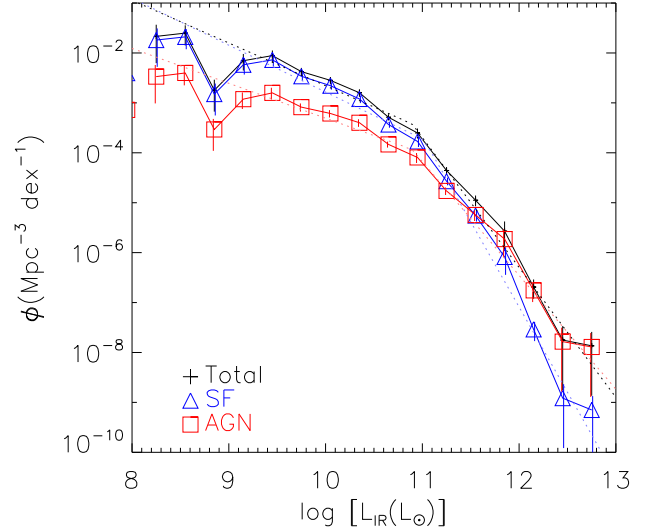


Figure 9. IR LF is separated for star-forming galaxies (blue triangles) and AGN (red squares) using Fig.8. Total IR LF is shown with the black plus sign. The dotted-lines are the best-fit double-power laws.

and $\Omega_{IR}^{SFG}(\text{LIRG}) \propto (1+z)^{5.3 \pm 2.0}$. $\Omega_{IR}^{SFG}(\text{ULIRG})$ shows more rapid evolution than $\Omega_{IR}^{SFG}(\text{LIRG})$, showing importance of luminous IR sources at high redshift.

5.3 Evolution of Ω_{IR}^{AGN}

In turn, we can also investigate the evolution of Ω_{IR}^{AGN} . This has been difficult in the literature since it is difficult to separate faint AGN individually in the presence of a host galaxy. By integrating IR LF_{AGN} in Fig.9, we obtained $\Omega_{IR}^{AGN} = 1.6^{+0.5}_{-0.3} \times 10^7 L_{\odot}\text{Mpc}^{-3}$.

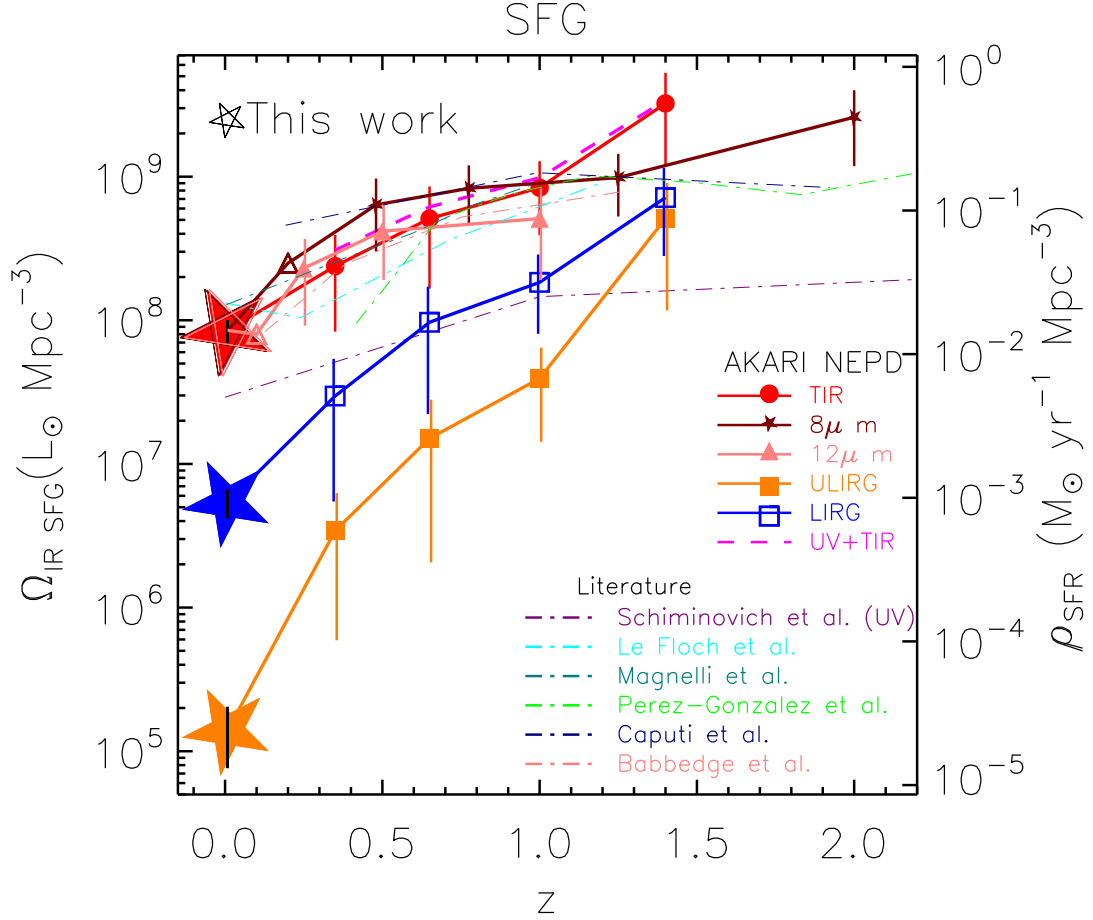


Figure 10. Evolution of TIR luminosity density by star-forming galaxies. Results from this work is plotted with triangles at $z=0.0082$. The red, blue and orange triangles show IR luminosity density from all galaxies, from LIRG only, and from ULIRG only. Higher redshift results in the solid lines are from the AKARI NEP deep field (Goto et al. 2010). Shown with different colors are TIR luminosity density based on TIR LFs (red circles), $8\mu\text{m}$ LFs (stars), and $12\mu\text{m}$ LFs (filled triangles). The blue open squares and orange filled squares are for only LIRG and ULIRGs, also based on our L_{TIR} LFs. Overplotted dot-dashed lines are estimates from the literature: Le Floch et al. (2005), Magnelli et al. (2009), Pérez-González et al. (2005), Caputi et al. (2007), and Babbedge et al. (2006) are in cyan, yellow, green, navy, and pink, respectively. The purple dash-dotted line shows UV estimate by Schiminovich et al. (2005). The pink dashed line shows the total estimate of IR (TIR LF) and UV (Schiminovich et al. 2005).

Kartaltepe et al. (2010) recently reported that the mean SED of $70\mu\text{m}$ -selected sample from the COSMOS survey at $z \sim 1$ is similar to what has been observed locally. As a natural consequence, the fraction of AGNs as a function of L_{IR} is in excellent agreement with that in the local universe (their Fig.30). If so, we can apply the $f_{AGN}-L_{IR}$ relation described in Fig.8 to IR LFs at higher redshifts to investigate the evolution of Ω_{IR}^{AGN} .

Practically, we applied the $f_{AGN}-L_{IR}$ relation in Fig.8 to IR LFs at $0 < z < 1.5$ presented by Goto et al. (2010) to obtain Ω_{IR}^{AGN} . Goto et al. (2010) used their own AGN/star-forming galaxy classification to remove AGN from their LFs, but for a fair comparison, we applied the same methodology as used in Section 5.1 to their LFs before they subtract the contribution from individual AGN.

In Fig.11, we show the evolution of Ω_{IR}^{AGN} , which shows a strong evolution with increasing redshift. At a first glance, both

Ω_{IR}^{AGN} and Ω_{IR}^{SFG} show rapid evolution, suggesting that the correlation between star formation and black hole accretion rate continues to hold at higher redshifts, i.e., galaxies and black holes seem to be evolving hand in hand. However, there are some differences as well. When we fit the evolution with $(1+z)^7$, we found $\Omega_{IR}^{AGN} \propto (1+z)^{4.4 \pm 0.4}$, which is possibly more rapid evolution than Ω_{IR}^{SFG} although errors are significant. The contribution by ULIRGs quickly increases toward higher redshift; By $z=1.5$, it exceeds that from LIRGs. Indeed, we found $\Omega_{IR}^{AGN}(ULIRG) \propto (1+z)^{9.4 \pm 0.8}$ and $\Omega_{IR}^{AGN}(LIRG) \propto (1+z)^{5.5 \pm 0.8}$.

It seems there is no sign of flattening at high redshift in $\Omega_{IR}^{AGN}(z)$. It would be interesting to compare this with a number-density evolution of optical QSOs (Croom et al. 2004; Richards et al. 2006), which peaks at $z=2-3$, and the evolution of X-ray AGN (Ueda et al. 2003; Hasinger, Miyaji, & Schmidt 2005). Aird et al. (2010) recently presented the evolution of X-ray lu-

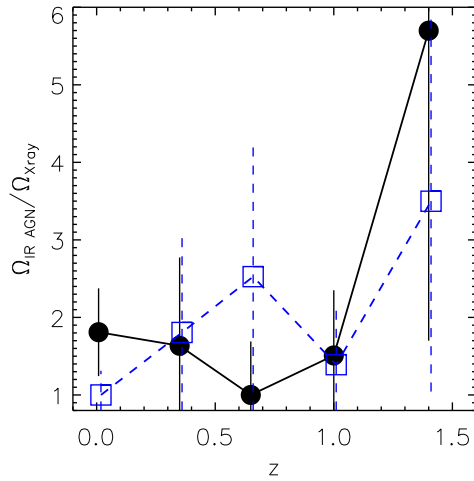


Figure 12. X-ray luminosity density to Ω_{IR}^{AGN} ratio is plotted as a function of redshift. The ratio is normalized at the minimum value. The X-ray luminosity densities of black circles and blue squares are from Aird et al. (2010) (2-10 keV) and Hasinger, Miyaji, & Schmidt (2005) (0.5-2 keV), respectively.

minosity density, which shows a turnover at around $z \sim 1.2 \pm 0.1$. In Fig.11, our Ω_{IR}^{AGN} does not show any sign of decline at least up to $z=1.5$, in contrast to the X-ray results. Barger et al. (2005) also showed much shallower evolution in X-ray than our IR results. In Fig.12, we investigate the evolution of X-ray luminosity density to Ω_{IR}^{AGN} ratio. X-ray luminosity densities are taken from Aird et al. (2010) Aird et al. (2010) (2-10 keV) and Hasinger, Miyaji, & Schmidt (2005) (0.5-2 keV). It is interesting that the ratio is consistent with a constant value at $0 < z < 1$, and shows a possible increase at $z > 1$, although it is unfortunate our errors are too large to draw a firm conclusion. The possible difference may suggest an increase of obscured AGN light toward higher redshift at $z > 1$ compared with optical/X-ray unobscured AGN. Post-starburst AGN galaxies found by Goto (2006) may be an example of such phenomena. Recently, Treister et al. (2010) showed an increase in the number ratio of obscured/unobscured QSOs with increasing redshift, concluding that a merger-driven black hole evolution model is consistent with the observed result. Our Fig.12 may suggest a similar obscured/unobscured AGN evolution in terms of AGN luminosity density, instead of the number density. A possible deviation from Ω_{IR}^{SFG} also suggests AGN may have formed earlier than star-formation in terms of infrared luminosity density. More accurate comparison of X-ray and IR luminosity density evolution of AGN will bring an interesting physical implication on the subject. In particular, reducing measurement errors at high redshift is urgent.

6 SUMMARY

Using AKARI's 6-band IR photometry in 9, 18, 65, 90, 140, and $160\mu m$ with much improved spatial resolution to resolve background cirrus/confusing sources, we have re-measured L_{TIR} of the RBGS through IR SED model fitting. This is a significant progress

considering that the IRAS used one linear equation to estimate L_{TIR} , with only data at $< 100\mu m$.

By using this new L_{TIR} measurement, we constructed local IR LFs separately for SFG and AGN. We also computed local infrared luminosity density through the derived LFs, and compared Ω_{IR}^{SFG} and Ω_{IR}^{AGN} to those at higher redshifts.

Our findings are as follows.

- SED model-to-model variation in estimating L_{TIR} is less than 25%.
- We present L_{MIR} -to- L_{TIR} conversions for Spitzer $8\mu m$, AKARI $9\mu m$, IRAS $12\mu m$, WISE $12\mu m$, ISO $15\mu m$, AKARI $18\mu m$, WISE $22\mu m$, and Spitzer $24\mu m$ filters. These conversions provides us with a useful tool to estimate L_{TIR} with a MIR band only.
- Re-constructed local TIR LF with the AKARI data is consistent with that from the IRAS, i.e., the AKARI's better data show the IRAS measurement was correct.
- By integrating the IR LF weighted by L_{TIR} , we obtain the local cosmic IR luminosity density of $\Omega_{TIR} = (8.5_{-2.3}^{+1.5}) \times 10^7 L_{\odot} \text{Mpc}^{-3}$.
- LIRG and ULIRG contribute to Ω_{TIR} a little; Only $7 \pm 1\%$ of Ω_{TIR} is produced by LIRG ($L_{TIR} > 10^{11} L_{\odot}$), and only $0.4 \pm 0.1\%$ is by ULIRG ($L_{TIR} > 10^{12} L_{\odot}$) in the local Universe, in stark contrast to high redshift results.
- Compared with high redshift results from the AKARI NEP deep survey, we observed a strong evolution of $\Omega_{TIR}^{SFG} \propto (1+z)^{4.0 \pm 0.5}$, after removing AGN contribution.
- We showed an evolution of Ω_{IR}^{AGN} scales as $\propto (1+z)^{4.4 \pm 0.4}$. ULIRG contribution to the Ω_{IR}^{AGN} exceeds that by LIRG by $z=1.5$.
- $\Omega_{IR}^{AGN}/\Omega_{X-ray}^{AGN}$ ratio shows a possible increase at $z > 1$. If confirmed, this may suggest an increase of obscured AGN at $z > 1$.

ACKNOWLEDGMENTS

We thank the anonymous referee for many insightful comments, which significantly improved the paper. We are indebted to M.Malkan for many valuable comments and suggestions. We thank D.Sanders and J.M. Mazzarella for useful discussions.

T.G. acknowledges financial support from the Japan Society for the Promotion of Science (JSPS) through JSPS Research Fellowships for Young Scientists.

This research is based on the observations with AKARI, a JAXA project with the participation of ESA.

The authors wish to recognize and acknowledge the very significant cultural role and reverence that the summit of Mauna Kea has always had within the indigenous Hawaiian community. We are most fortunate to have the opportunity to conduct observations from this sacred mountain.

Support for the work of ET was provided by the National Aeronautics and Space Administration through Chandra Postdoctoral Fellowship Award Number PF8-90055 issued by the Chandra X-ray Observatory Center, which is operated by the Smithsonian Astrophysical Observatory for and on behalf of the National Aeronautics Space Administration under contract NAS8-03060.

TTT has been supported by Program for Improvement of Research Environment for Young Researchers from Special Coordination Funds for Promoting Science and Technology, and the Grant-in-Aid for the Scientific Research Fund (20740105) commissioned by the Ministry of Education, Culture, Sports, Science and Technology (MEXT) of Japan. TTT has been also partially supported from the Grand-in-Aid for the Global COE Program "Quest for

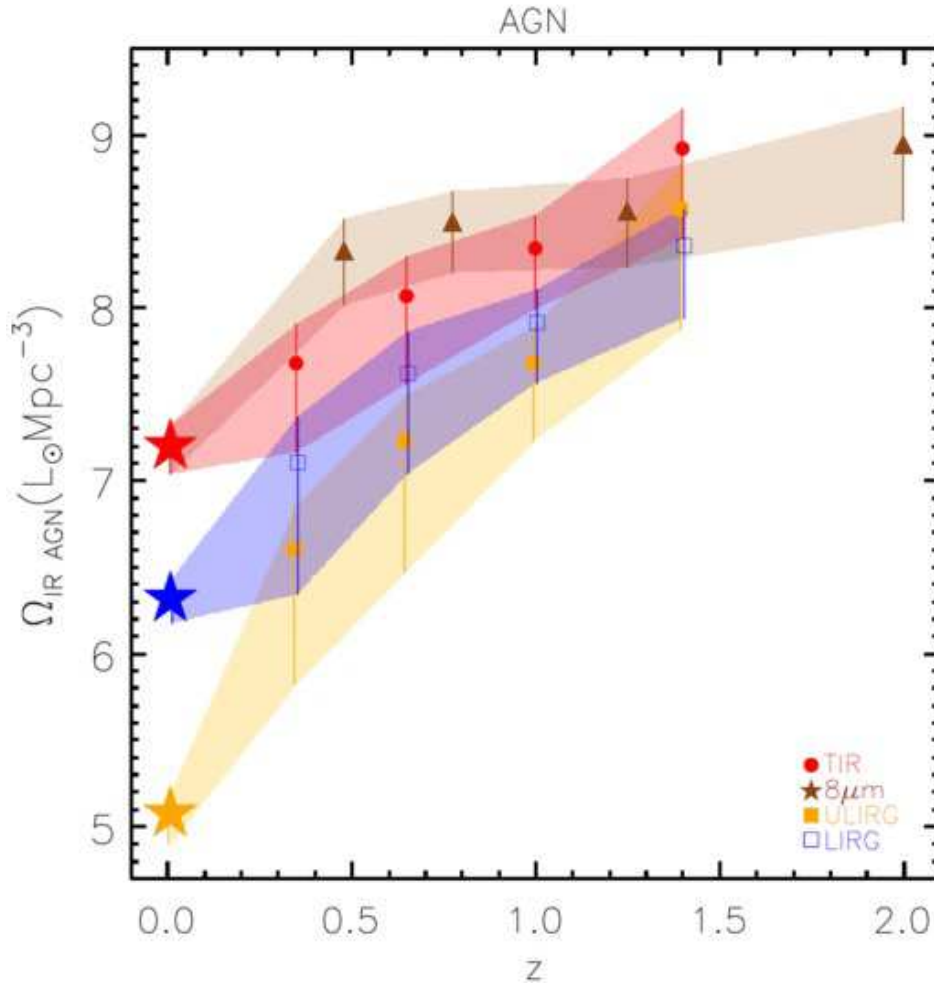


Figure 11. Evolution of TIR luminosity density by AGN. Results from this work is plotted with stars at $z=0.0082$. The red, blue and orange points show IR luminosity density from all AGN, from LIRG AGN only, and from ULIRG AGN only. Higher redshift results are from the AKARI NEP deep field (Goto et al. 2010), with contribution from star forming galaxies removed. Brown triangles are $\Omega_{\text{IR}}^{\text{AGN}}$ computed from the $8\mu\text{m}$ LFs (Goto et al. 2010).

Fundamental Principles in the Universe: from Particles to the Solar System and the Cosmos” from the MEXT.

REFERENCES

- Aird J., et al., 2010, MNRAS, 401, 2531
 Babbedge T. S. R., et al., 2006, MNRAS, 370, 1159
 Barger A. J., Cowie L. L., Mushotzky R. F., Yang Y., Wang W.-H., Steffen A. T., Capak P., 2005, AJ, 129, 578
 Bavouzet N., Dole H., Le Floc’h E., Caputi K. I., Lagache G., Kochanek C. S., 2008, A&A, 479, 83
 Boquien M., et al., 2010, ApJ, 713, 626
 Caputi K. I., et al., 2007, ApJ, 660, 97
 Chary R., Elbaz D., 2001, ApJ, 556, 562
 Croom S. M., Smith R. J., Boyle B. J., Shanks T., Miller L., Outram P. J., Loaring N. S., 2004, MNRAS, 349, 1397
 Dale D. A., Helou G., 2002, ApJ, 576, 159
 Dunne L., Eales S. A., 2001, MNRAS, 327, 697
 Gandhi P., Horst H., Smette A., Höning S., Comastri A., Gilli R., Vignali C., Duschl W., 2009, A&A, 502, 457
 Goto T., et al., 2010, A&A, 514, A6
 Goto T., 2006, MNRAS, 369, 1765
 Goto T., 2005, MNRAS, 360, 322
 Gruppioni C., et al., 2010, A&A, 518, L27
 Hasinger G., Miyaji T., Schmidt M., 2005, A&A, 441, 417
 Ishihara D., et al., 2010, A&A, AKARI special issue in press
 Jeong W.-S., et al., 2007, PASJ, 59, 429
 Kartaltepe J. S., et al., 2010, ApJ, 709, 572
 Kennicutt R. C., Jr., 1998, ARA&A, 36, 189
 Kewley L. J., Groves B., Kauffmann G., Heckman T., 2006, MNRAS, 372, 961
 Lagache G., Dole H., Puget J.-L., 2003, MNRAS, 338, 555
 Le Floc’h E., et al., 2005, ApJ, 632, 169
 Magnelli B., Elbaz D., Chary R. R., Dickinson M., Le Borgne D., Frayer D. T., Willmer C. N. A., 2009, A&A, 496, 57
 Mould J. R., et al., 2000, ApJ, 529, 786
 Murakami H., et al., 2007, PASJ, 59, 369
 Pérault M., 1987, PhDT,
 Pérez-González P. G., et al., 2005, ApJ, 630, 82
 Pozzi F., et al., 2004, ApJ, 609, 122

- Richards G. T., et al., 2006, *AJ*, 131, 2766
Rodighiero G., et al., 2010, *A&A*, 515, A8
Rush, B., Malkan, M., Spinoglio, L., 1993, *ApJS*, 89, 1
Sanders D. B., Mazzarella J. M., Kim D.-C., Surace J. A., Soifer
B. T., 2003, *AJ*, 126, 1607
Saunders W., Rowan-Robinson M., Lawrence A., Efstathiou G.,
Kaiser N., Ellis R. S., Frenk C. S., 1990, *MNRAS*, 242, 318
Schiminovich D., et al., 2005, *ApJ*, 619, L47
Schmidt M., 1968, *ApJ*, 151, 393
Siebenmorgen R., Krügel E., 2007, *A&A*, 461, 445
Spinoglio, L., Malkan, Rush, B., Carrasco, L., Recillas-Cruz, E.,
1995, *ApJ*, 435, 616
Smith J. D. T., et al., 2007, *ApJ*, 656, 770
Symeonidis M., Page M. J., Seymour N., Dwelly T., Coppin K.,
McHardy I., Rieke G. H., Huynh M., 2009, *MNRAS*, 397, 1728
Takeuchi T. T., Yoshikawa K., Ishii T. T., 2000, *ApJS*, 129, 1
Takeuchi T. T., Yoshikawa K., Ishii T. T., 2003, *ApJ*, 587, L89
Takeuchi T. T., Buat V., Iglesias-Páramo J., Boselli A., Burgarella
D., 2005, *A&A*, 432, 423
Takeuchi T. T., Ishii T. T., Dole H., Dennefeld M., Lagache G.,
Puget J.-L., 2006, *A&A*, 448, 525
Takeuchi T.T., et al., 2010, *A&A*, AKARI special issue in press
Treister E., et al. 2010, *Science* in press
Treister E., Urry C. M., Virani S., 2009, *ApJ*, 696, 110
Ueda Y., Akiyama M., Ohta K., Miyaji T., 2003, *ApJ*, 598, 886
Wright E. L., 2008, *EAS*, 33, 57
Yamamura I., et al., 2009, *AIPC*, 1158, 169
Yuan T.-T., Kewley L. J., Sanders D. B., 2010, *ApJ*, 709, 884